

"This document is the unedited Author's version of a Submitted Work that was subsequently accepted for publication in Nano Letters, copyright © American Chemical Society after peer review. To access the final edited and published work see <http://pubs.acs.org/doi/abs/10.1021/nl2005143>."

Single-Photon Detectors Based on Ultranarrow Superconducting Nanowires

Francesco Marsili,^{*,†} Faraz Najafi,[†] Eric Dauler,[‡] Francesco Bellei,[†] Xiaolong Hu,[†] Maria Csete,[†] Richard J. Molnar,[‡] and Karl K. Berggren^{†,§}

[†]Department of Electrical Engineering and Computer Science, Massachusetts Institute of Technology, 77 Massachusetts Avenue, Cambridge, Massachusetts 02139, United States

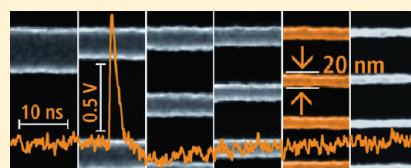
[‡]Lincoln Laboratory, Massachusetts Institute of Technology, 244 Wood Street, Lexington, Massachusetts 02420, United States

[§]Kavli Institute of Nanoscience, Delft University of Technology, Lorentzweg 1, 2628CJ Delft, The Netherlands

S Supporting Information

ABSTRACT: We report efficient single-photon detection ($\eta = 20\%$ at 1550 nm wavelength) with ultranarrow (20 and 30 nm wide) superconducting nanowires, which were shown to be more robust to constrictions and more responsive to 1550 nm wavelength photons than standard superconducting nanowire single-photon detectors, based on 90 nm wide nanowires. We also improved our understanding of the physics of superconducting nanowire avalanche photodetectors, which we used to increase the signal-to-noise ratio of ultranarrow-nanowire detectors by a factor of 4, thus relaxing the requirements on the read-out circuitry and making the devices suitable for a broader range of applications.

KEYWORDS: Superconducting nanowire single-photon detectors, SNSPDs



Superconducting nanowire single-photon detectors (SNSPDs)¹ perform single-photon counting with exceptional sensitivity and time resolution at near-infrared wavelengths.² State-of-the-art SNSPDs, based on 100 nm wide, 4–5 nm thick NbN nanowires,² are vulnerable to constrictions,³ which significantly limit their yield. Also, their detection efficiency becomes negligible beyond 2 μm wavelength,⁴ which makes them unsuitable for mid-infrared applications.^{5–9} SNSPDs based on few-tens-of-nanometer-wide nanowires are expected to efficiently detect mid-infrared photons and to operate at low bias currents,^{4,10,11} so constrictions may have less impact on their performance. Prior to this work, SNSPDs based on nanowires narrower than 50 nm³ had not been demonstrated due to two factors: (1) the SNSPD signal is roughly proportional to the nanowire width,¹ so narrow nanowires have poor signal-to-noise ratio; (2) fabrication at these length scales is extremely challenging. In this Letter we report on how we addressed these issues and demonstrated efficient single-photon detection (20% detection efficiency at 1550 nm wavelength) with detectors based on ultranarrow (30 and 20 nm wide) nanowires.

We have demonstrated that 30 nm nanowire-width SNSPDs are more responsive to 1550 nm wavelength photons and more robust with respect to constrictions than previous detectors.

We fabricated SNSPDs based on 30 nm wide nanowires free of geometrical constrictions for over 10 μm length (Figure 1a) and measured the device detection efficiency (η) at 1550 nm wavelength (λ) and the dark count rate (DCR) as a function of the bias current (I_B) of ~ 200 detectors across six fabrication runs.

The detection efficiency of our 30 nm nanowire-width SNSPDs showed a sigmoidal dependence on I_B (Figure 1b), saturating at $\sim 18\%$ above a cutoff current $I_{co} \sim 0.5 I_C$ (the nanowire critical current), while as a comparison, 90 nm nanowire-width SNSPDs did

not reach the I_{co} (Figure 1b). To quantify the spectral responsivity of these devices, we used the ratio between the detection efficiency at I_{co} and the normalized cutoff current (I_{co}/I_C) at a certain wavelength: $r = \eta_{I_{co}}/(I_{co}/I_C)$. According to this figure of merit, ultranarrow-nanowire SNSPDs showed much higher responsivity to 1550 nm wavelength photons ($r = 16.3$) than previous detectors ($r = 9.6$, assuming $I_{co} = I_{sw}$) as they could reach the same detection efficiency with a lower bias relative to I_C . As the I_{co} is known to shift to higher currents for longer wavelengths,¹² these results suggest that the sensitivity of ultranarrow-nanowire SNSPDs extends further into the mid-infrared range than the sensitivity of standard SNSPDs. Furthermore, due to the low I_{co} of 30 nm nanowire-width SNSPDs, even a heavily constricted device could reach approximately the same detection efficiency as a constriction-free device, while the detection efficiencies of 90 nm nanowire-width SNSPDs with the same absolute and relative constriction were about 30% and 10 times lower than a constriction-free device (Figure 1b).

As the SNSPD photoresponse amplitude is proportional to its bias current¹ and our 30 nm nanowire-width devices had a switching current about three times lower than the 90 nm nanowire-width devices, they exhibited a correspondingly lower signal and a signal-to-noise ratio (SNR, the ratio of the photoresponse pulse amplitude and the noise peak amplitude) ranging from 1.5 to 3.5. The device sensitivity was then strongly dependent on the somewhat arbitrary level of the discriminator trigger used to count the photoresponse pulses. Although we could minimize the counts triggered by the electrical noise (we call these counts *false counts*

Received: February 12, 2011

Revised: March 7, 2011

Published: April 01, 2011

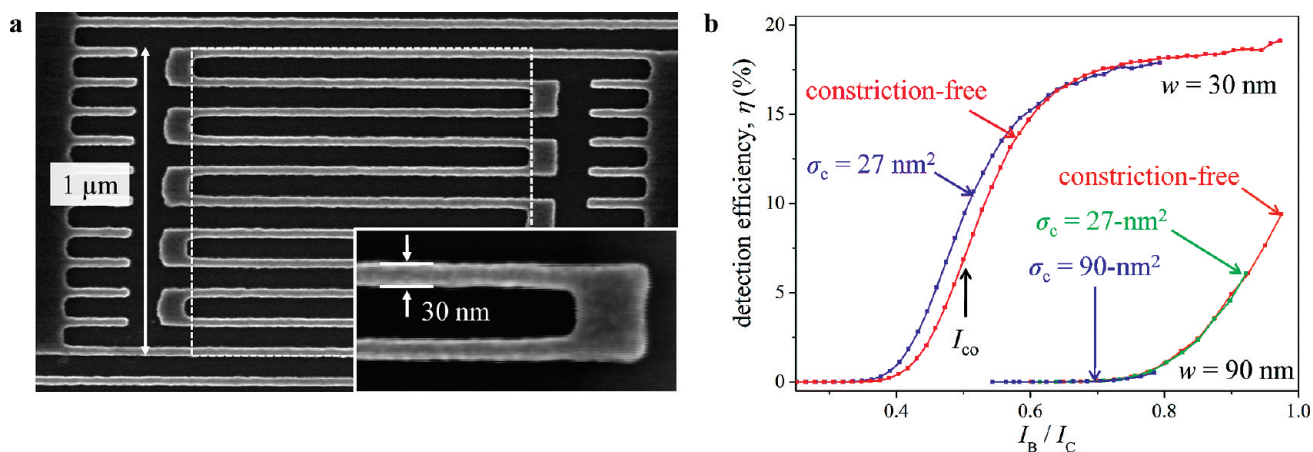


Figure 1. SNSPDs based on 30 nm wide nanowires. (a) Scanning electron microscope (SEM) images of an SNSPD hydrogen silsesquioxane (HSQ) mask on NbN. The nanowires are 30 nm wide and the pitch is 100 nm (inset), covering an active area of $1.03 \mu\text{m} \times 1.14 \mu\text{m}$ (dashed frame). See Supporting Information for the device fabrication process. (b) Device detection efficiency at $\lambda = 1550 \text{ nm}$ as a function of normalized bias current for constricted and constriction-free SNSPDs based on 30 nm wide and 90 nm wide nanowires. We assumed the constriction to be a reduction of the nanowire superconducting cross-sectional area with respect to the nominal value. We quantified the device constriction state by estimating the area of the nonsuperconducting part of the nanowire cross section as $\sigma_c = \sigma_n(1 - I_{\text{SW}}/I_C)$, where σ_n is the nominal nanowire cross section, estimated from the nanowire width (measured by SEM) and thickness (estimated from the material deposition time and rate), I_{SW} is the device switching current, defined as the bias current at which the device switches from the superconducting to the normal state, and I_C is the device critical current, experimentally defined as the highest measured I_{SW} of the devices fabricated on the same film for the ultranarrow-nanowire SNSPDs ($I_C = 7.2 \mu\text{A}$) and extracted from kinetic inductance vs I_B measurements³ for the 90 nm nanowire-width SNSPDs ($I_C = 18.8\text{--}20.1 \mu\text{A}$). The device detection efficiency was calculated as $\eta = H(\text{CR} - \text{DCR})/N_{\text{ph}}$, where CR is the count rate measured when the SNSPD was illuminated, DCR is the count rate measured when the SNSPD was not illuminated, H is a normalization factor (see Supporting Information), and N_{ph} is the number of photons per second incident on the device active area. The I_{co} (defined to be at the inflection point of the η vs I_B curves) of the 30 nm wide nanowire-width SNSPDs is marked with a black arrow (see Supporting Information).

to distinguish them from true dark counts, triggered by the detector) when targeting a specific detection efficiency, it was not possible to eliminate them without sacrificing η (see Supporting Information).

To address the issue of low SNR affecting ultranarrow-nanowire SNSPDs without employing elaborate SQUID-based read-out schemes,¹³ we studied superconducting nanowire avalanche photodetectors (SNAPs).¹⁴ Our investigation led to three key results: (1) the discovery of novel operation regimes of SNAPs; (2) the understanding of the working principle of these devices; and (3) the demonstration of an increase in SNR of a factor of 4—sufficient to negate the effect of false counts.

An N -SNAP is the parallel connection of N nanowires (Figure 2a) and can provide a photoresponse pulse with N -times-larger amplitude than an SNSPD. The device is connected in series with an inductor (L_S) and in parallel with a read-out resistor (R_{load} , Figure 2b). All the sections have nominally the same kinetic inductance (L_0), so at the steady state they should be biased at the same current (I_B/N). When one section switches to the normal state after absorbing a photon (initiating section), part of its current is redistributed among the still-superconducting sections (secondary sections) and R_{load} . The theoretical working principle of SNAPs is that,¹⁴ if I_B is higher than a threshold value (the avalanche current, I_{AV}), the current from the initiating section switches all of the secondary sections to the normal state, so that most of the current flowing through the device ($\sim N$ times larger than the current carried by a single section) is diverted to the read-out.

According to the analysis of the device operation conducted so far,¹⁴ the initiating section redistributes all of its current to the secondary sections (we called this assumption *perfect redistribution*). As this simplified analysis did not fit the experimental data,¹⁵ we developed an alternative model of SNAPs, based on the

electrothermal simulation of each section of the device.¹⁶ Performing simulations at different values of I_B (Figure 2c and d), we estimated I_{AV} for each value of N . As the electrothermal model predicts that the initiating section switches back to the superconducting state before being completely depleted of its current (Figure 2d), higher bias currents are required to trigger an avalanche than expected by assuming perfect redistribution (Figure 2e).

To assess the validity of our model, we fabricated and characterized 30 nm nanowire-width SNAPs designed to have two to four sections in parallel (~ 200 devices across four fabrication runs).

We measured DCR and η of our devices as a function of I_B (Figure 3a). The η vs I_B curve of 2-SNAPs showed a classic sigmoidal shape, as observed for SNSPDs. However, the η vs I_B curves of 3- and 4-SNAPs showed three inflections before overlapping with the curves of the other devices. Following ref 15, we defined the experimental SNAP avalanche current to be at the first inflection point of the η vs I_B curves ($I_B = I_1$, see Supporting Information), but the values of I_{AV} we obtained from this approach (Figure 2e) could not be fitted by any of the models discussed so far.

To gain better insight on the device operation, we measured η at different light intensities and the jitter as a function of I_B for 3- and 4-SNAPs (Figure 3b–e). As expected for a single-photon detector, η was independent of the photon flux (μ) at bias currents exceeding the highest inflection point (Figure 3b and c), as the detector count rate increased linearly with μ (see inset of Figure 3b). However, at lower bias η unexpectedly decreased when increasing μ , as the count rate had a sublinear dependence on μ (inset of Figure 3b). The jitter vs I_B curves exhibited one (3-SNAP, Figure 3d) or two (4-SNAP, Figure 3e) abrupt discontinuities. These data suggested that radical changes in the device operation took place as the bias current was varied.

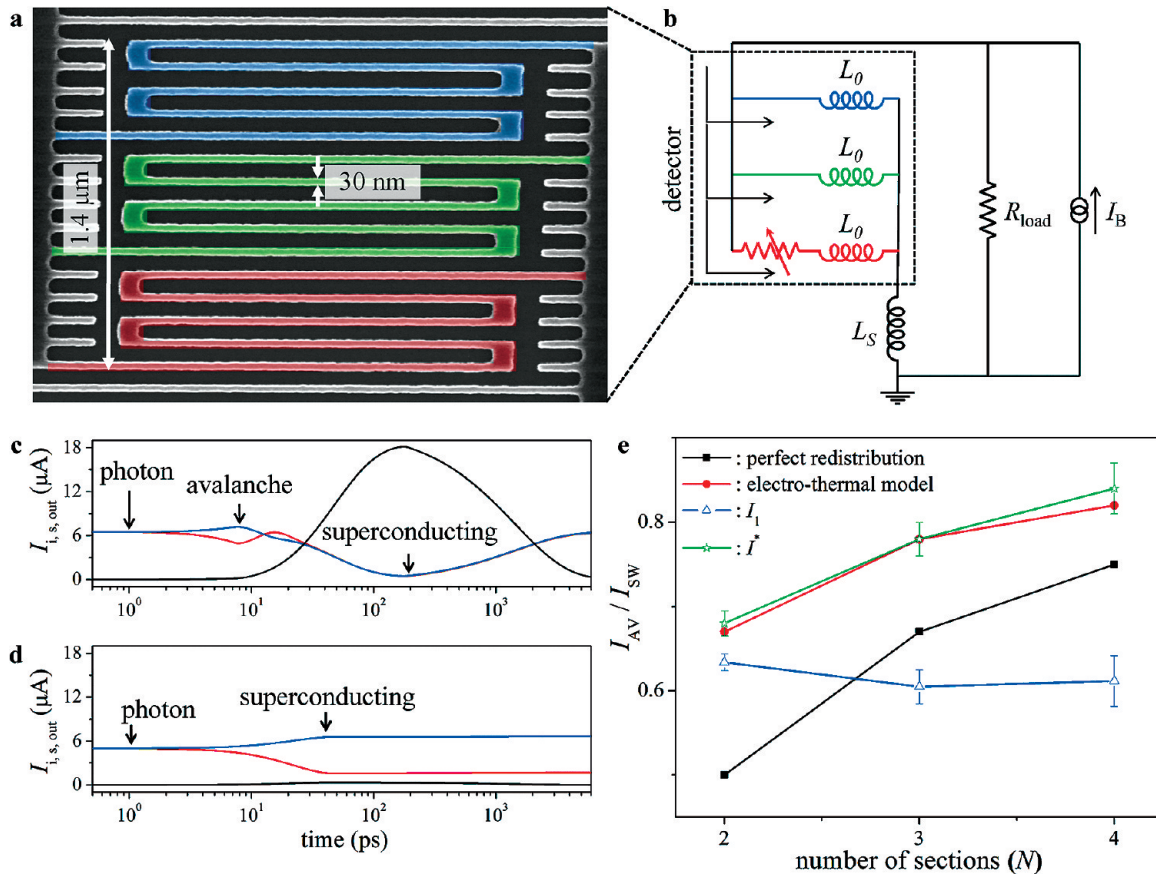


Figure 2. Superconducting nanowire avalanche photodetectors (SNAPs). (a) Colorized SEM image of a 3-SNAP resist (HSQ) mask on NbN with each section colored differently. (b) Equivalent electrical circuit of a 3-SNAP. (c, d) Electrothermal simulation of the current dynamics after photodetection through R_{load} (I_{out} in black), through the initiating section (I_i in red), and through the two secondary sections (I_s in blue, identical) of a 3-SNAP at different I_B (see ref 16 for details on the model). At “high” bias ($I_B = 0.9 I_{\text{SW}}$, Figure 2c), the current redistribution is sufficient to trigger an avalanche. Arrows mark the instants at which the initiating section switches to the normal state after absorbing a photon (arrow labeled “photon”), the avalanche starts (arrow labeled “avalanche”), and the initiating section switches back to the superconducting state (arrow labeled “superconducting”). Note that the amplitude of the current pulse through R_{load} is about three times higher than the bias current through a single section. At “low” bias ($I_B = 0.7 I_{\text{SW}}$, Figure 2d), the current redistribution in the secondary sections is not sufficient to make them switch, so no avalanche is triggered. (e) $I_{\text{AV}}/I_{\text{SW}}$ vs N calculated by assuming perfect redistribution (in black, see Supporting Information) and simulated by using the electrothermal model (in red). First-inflection current (I_1 , in blue) and intensity-independent current (I^* , in green) extrapolated from the η vs I_B curves presented in Figure 3a–c. We took the experimental error on the values of I_1 and I^* (see error bars) to be twice the step size at which the η vs I_B curves were acquired.

We developed a new model of the SNAP operation at different bias currents, which qualitatively agrees with the experimental results of Figure 3b–e.

In this model, we assumed that the current at which η became independent of intensity (I^* , see Supporting Information) was the true SNAP avalanche current. For $I_B > I^*$, each hot-spot nucleation (HSN) event (due to either a dark count or a photon absorption) triggers an avalanche (Figure 2c). For $I_1 < I_B < I^*$, two subsequent HSN events (which we named “arm” and “trigger”) are necessary to create one avalanche. To illustrate the arm-trigger regime, we modeled a 3-SNAP biased below its I_{AV} (Figure 4a). After the first HSN event (arm), the current redistributes from the initiating section and biases the secondary sections very close to their I_{SW} . At this point, the 3-SNAP behaves as a pseudo-2-SNAP, biased above its I_{AV} , so a second HSN event (trigger) in one of the remaining sections can trigger the avalanche.

This model does not clarify why the jitter increases with decreasing I_B , but it suggests a root cause for the steps in the jitter vs I_B curves shown in panels d and e of Figure 3. Indeed, we can

reasonably suppose that as the bias current was decreased below I^* , the devices transitioned from operating as 3-SNAPs (4-SNAPs), biased slightly above I_{AV} (in a high-jitter regime), to operating as pseudo-2-SNAPs (3-SNAPs), biased far above I_{AV} (in a low-jitter regime). We attribute the second jitter step measured only for 4-SNAPs to the fact that these devices further transitioned to operating as pseudo-2-SNAPs.¹⁷ Our model also qualitatively explains the intensity dependence of η for $I_1 < I_B < I^*$. Indeed, at high photon fluxes, it is more likely that both the arm and trigger events are photon absorptions so that not every absorbed photon results in an avalanche, while at low photon fluxes, only one photon absorption may suffice to create an avalanche, as a dark count event may occur before another photon is absorbed.

To quantitatively support our model, we measured the histograms of the avalanche interarrival time of a 4-SNAP biased above and below I^* (Figure 4b). The two histograms are radically different and are each independently in close agreement with the avalanche interarrival time probability distributions calculated from the experimental values of η , μ , and DCR by assuming in

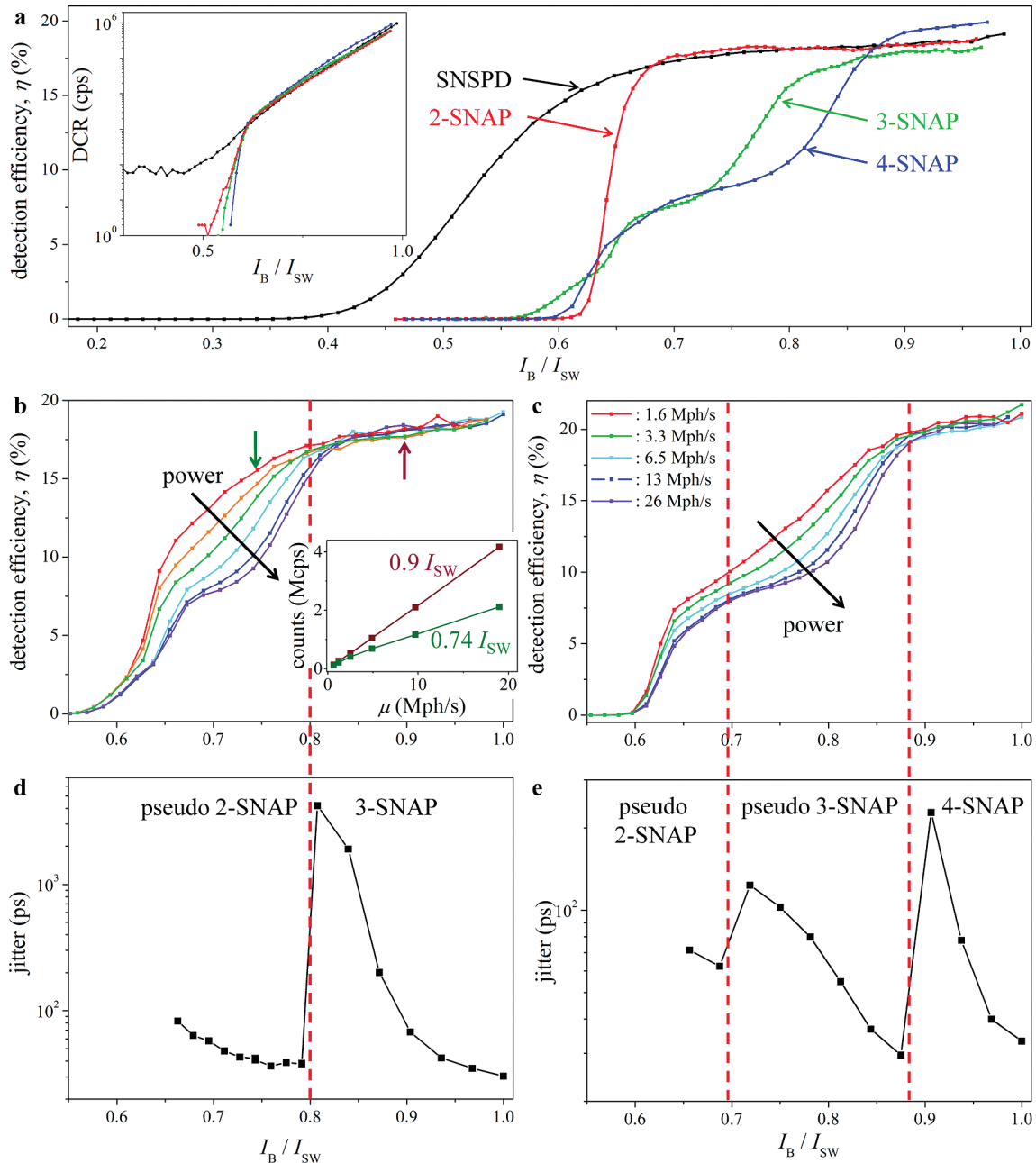


Figure 3. Detection efficiency and jitter of SNAPs vs normalized bias current. (a) η at 1550 nm wavelength and DCR (inset) vs normalized bias current (ratio of bias current and switching current of each device, I_B/I_{SW}) for an SNSPD, a 2-SNAP, a 3-SNAP, and a 4-SNAP based on 30 nm wide nanowires (in black, red, green, and blue, respectively). The devices were designed by integrating in parallel the same $1.47 \mu\text{m} \times 230 \text{ nm}$ section $N = 1, 2, 3, 4$ times. The series inductance of the N -SNAPs was designed to satisfy the condition $L_S(N-1)/L_0 = 10$, where $L_0 = 13 \text{ nH}$ is the kinetic inductance of one section (estimated from the fall time of the SNSPD response pulse). The detector switching currents were $I_{SW} = 7.2 \mu\text{A}$ (SNSPD); $13.4 \mu\text{A}$ (2-SNAP); $18.1 \mu\text{A}$ (3-SNAP); $28.4 \mu\text{A}$ (4-SNAP). The photon fluxes (expressed in photons per second, photons/s) on the detector active area were $\mu = 5.5 \text{ Mphotons/s}$ (SNSPD); 12 Mphotons/s (2-SNAP); 19 Mphotons/s (3-SNAP); 25 Mphotons/s (4-SNAP). (b, c) η vs I_B/I_{SW} of the 3-SNAP (b) and 4-SNAP (c) of panel a under different illumination conditions. (b, inset) Detector count rate (CR - DCR) vs photon flux for the 3-SNAP of Figure 3b biased above ($I_B = 0.9 I_{SW}$, dark red) and below ($I_B = 0.74 I_{SW}$, dark green) the highest inflection point of the η vs I_B curve (see dark red and dark green arrows in panel b). (d, e) Jitter as a function of the normalized bias current of a 3-SNAP (d) and a 4-SNAP (e). We defined the jitter as the full width at half-maximum of the instrument response function (IRF). See Supporting Information for further details.

the first case that one avalanche was created by each HSN event and in the second case by two subsequent HSN events. This agreement between theory and experiment with no free parameters supported the validity of our model and justified our identification of I_{AV} with I^* . The experimental values of I_{AV}

obtained with our convention were in close agreement with the results of the electrothermal model (Figure 2e), which provided further support to our operational model of the device. We could therefore conclude that while in avalanche regime SNAPs operated as standard single-photon detectors, in arm-trigger

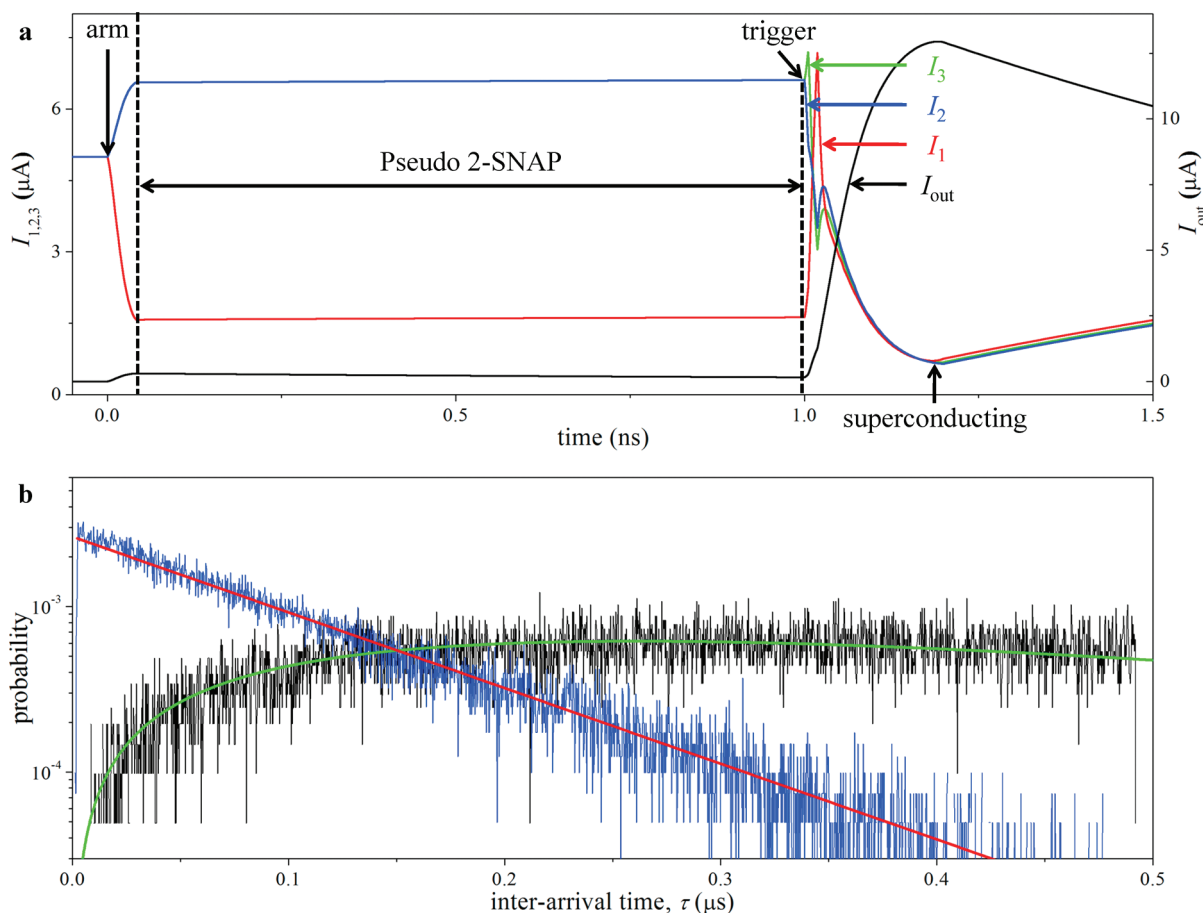


Figure 4. SNAP operation mechanism. (a) Electrothermal simulation of the current through the read-out resistor (I_{out} in black) and the sections of a 3-SNAP ($I_{1,2,3}$, in red, blue, and green, respectively) biased below I_{AV} . One HSN event was set to happen in section 1 at time = 0 s (arm event) and another in section 2 at time = 1 ns (trigger event). (b) Histograms of the avalanche interarrival time (the time between the arrival of two subsequent avalanches) of a 4-SNAP illuminated with a continuous wave laser emitting at 1550 nm (see Supporting Information) operating in avalanche regime ($I_B = 0.98 I_{SW}$, in blue) and in arm-trigger regime ($I_B = 0.78 I_{SW}$, in black). Plots of the interarrival time probability distribution generated with equations (S.1) (in red) and (S.2) (in green) in Supporting Information by using the experimental values of η , μ , and DCR and no free parameters. The device detection efficiency was $\eta = 18\%$; the photon fluxes were $\mu = 48$ Mphotons/s (blue and red curves) and 24 Mphotons/s (black and green curves); the dark count rates (dominated by background light) were DCR = 1.7 Mcounts/s (blue and red curves) and 81 kcounts/s (black curve).

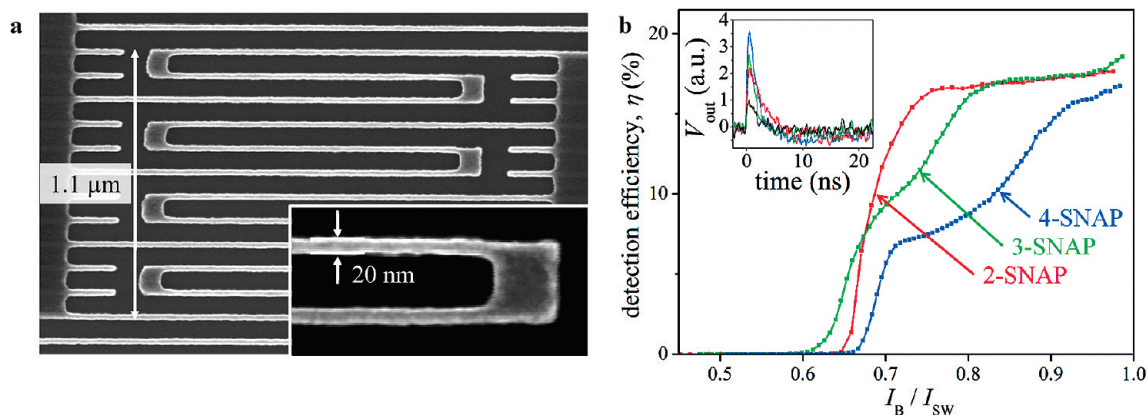


Figure 5. SNAPs based on 20 nm wide nanowires. (a) SEM image of a 4-SNAP resist (HSQ) mask on NbN. The nanowires were 20 nm wide and the pitch was 100 nm. The active area (defined as in Figure 1a) was $1.4 \mu\text{m}^2$. (b) η at 1550 nm wavelength as a function of the normalized bias current (ratio of bias current and switching current of each device, I_B/I_{SW}) for a 2-, 3-, and 4-SNAP (in red, green, and blue, respectively). The devices were designed by integrating in parallel the same $1.22 \mu\text{m} \times 220$ nm section $N = 2, 3, 4$ times. The series inductance of the N -SNAPs was designed to satisfy the condition $L_S(N-1)/L_0 = 10$. The detector switching currents were $I_{SW} = 8.4 \mu\text{A}$ (2-SNAP); $15.1 \mu\text{A}$ (3-SNAP); $18.1 \mu\text{A}$ (4-SNAP). Inset. Single-shot oscilloscope traces of the photoresponse pulse of an SNSPD, a 2-SNAP, a 3-SNAP, and a 4-SNAP based on 20 nm wide nanowires (in black, red, green, and blue, respectively), showing the improved SNR achieved by increasing the number of parallel sections of SNAPs. The devices were biased at $I_B = 0.9 I_{SW}$. The curves are normalized by the maximum amplitude of the SNSPD pulse.

regime they operated as multiphoton counters, responding with a single pulse to a sequence of two or three HSN events.

Using SNAPs we could read out the photoresponse of 20 nm wide nanowire (Figure 5a). The SNR of 20 nm nanowire-width SNSPDs was ~ 1.5 maximum, which resulted in unacceptably frequent false counts. However, with 2-, 3-, and 4-SNAPs it was possible to increase the SNR by factors of ~ 2 , 3, and 4, respectively (inset of Figure 5b) and achieve $\eta \sim 17\%$ (Figure 5b) and negligible false counts ($< 10^{-2}$ counts/s). The sensitivity of 20 nm wide nanowires is expected to extend to even longer wavelengths than 30 nm wide nanowires.¹⁰

In conclusion, we demonstrated efficient single-photon detection ($\eta = 17\text{--}20\%$ at 1550 nm wavelength) with 20 and 30 nm wide superconducting nanowires, which showed to be more responsive to 1550 nm wavelength photons and more robust to constrictions than wider nanowires. We also improved our understanding of the physics of the SNAP device concept and quantitatively characterized the trade-off existing between the SNAP SNR (which increases with the number of sections in parallel N) and the bias-current range in which they operate as low-jitter single-photon detectors (which decreases with increasing N). Finally, we used SNAPs to increase the signal-to-noise ratio of ultranarrow-nanowire detectors by a factor of 4, thus relaxing the requirements on the read-out circuitry and making the devices suitable for a broader range of applications.

■ ASSOCIATED CONTENT

S Supporting Information. (1) Fabrication methods, (2) normalization method used to calculate the detection efficiency, (3) experimental definitions of I_{cov} , I_{J} , and I^* , (4) SNR and sensitivity of ultranarrow-nanowire detectors, (5) derivation of I_{AV} assuming perfect redistribution, (6) measurement setup, (7) derivation of the interarrival time probability distributions, (8) experimental procedure for jitter measurements, and (9) experimental definition of the detector dead time. This material is available free of charge via the Internet at <http://pubs.acs.org>.

■ AUTHOR INFORMATION

Corresponding Author

*E-mail: marsili@mit.edu. Department of Electrical Engineering and Computer Science, Massachusetts Institute of Technology, 50 Vassar St., Cambridge, MA 02139, United States.

■ ACKNOWLEDGMENT

The authors thank Hyunil Byun, James Daley, Mark Mondol, and Professor Rajeev Ram for technical support and Dr. Vikas Anant, Lin Lee Cheung, and Dr. Joel Yang for useful scientific discussions. This work was completed while Professor K. K. Berggren was supported by the Netherlands Organization for Scientific Research. The initial phases of the work at the MIT campus were sponsored by the National Science Foundation under NSF award no. ECCS-0823778. The later phases, including jitter measurements and device modeling, were supported by the Center for Excitonics, an Energy Frontier Research Center funded by the U.S. Department of Energy, Office of Science, Office of Basic Energy Sciences under Award Number DE-SC000 1088 (which supported Francesco Marsili and Xiaolong Hu). The work at MIT Lincoln Laboratory was sponsored by the United States Air Force under Air Force Contract FA8721-05-C-0002. Opinions, interpretations, recommendations, and conclusions are

those of the authors and are not necessarily endorsed by the United States Government.

■ REFERENCES

- (1) Gol'tsman, G. N.; Okunev, O.; Chulkova, G.; Lipatov, A.; Semenov, A.; Smirnov, K.; Voronov, B.; Dzardanov, A.; Williams, C.; Sobolewski, R. Picosecond superconducting single-photon optical detector. *Appl. Phys. Lett.* **2001**, *79* (6), 705–707.
- (2) Hadfield, R. H. Single-photon detectors for optical quantum information applications. *Nat. Photonics* **2009**, *3* (12), 696–705.
- (3) Kerman, A. J.; Dauler, E. A.; Yang, J. K. W.; Rosford, K. M.; Anant, V.; Berggren, K. K.; Gol'tsman, G. N.; Voronov, B. M. Constriction-limited detection efficiency of superconducting nanowire single-photon detectors. *Appl. Phys. Lett.* **2007**, *90* (10), 101110.
- (4) Korneeva, Y.; Florya, I.; Semenov, A.; Korneev, A.; Gol'tsman, G., New Generation of Nanowire NbN Superconducting Single-Photon Detector for Mid-Infrared. *IEEE Trans. Appl. Supercond.* **2010**, *PP* (99), 1–1.
- (5) Temporão, G.; Tanzilli, S.; Zbinden, H.; Gisin, N.; Aellen, T.; Giovannini, M.; Faist, J. Mid-infrared single-photon counting. *Opt. Lett.* **2006**, *31* (8), 1094–1096.
- (6) Measures, R. *Laser Remote Chemical Analysis*; John Wiley & Sons: New York, 1988.
- (7) Ippolito, S. B.; Thorne, S. A.; Eraslan, M. G.; Goldberg, B. B.; Unlu, M. S.; Leblebici, Y. High spatial resolution subsurface thermal emission microscopy. *Appl. Phys. Lett.* **2004**, *84* (22), 4529–4531.
- (8) Barbieri, C.; Dravins, D.; Occhipinti, T.; Tamburini, F.; Naletto, G.; deppo, V. D.; Fornasier, S.; D'Onofrio, M.; Fosbury, R. A. E.; Nilsson, R.; Uthas, H. Astronomical applications of quantum optics for extremely large telescopes. *J. Mod. Opt.* **2007**, *54* (2), 191–197.
- (9) Martini, R.; Bethea, C.; Capasso, F.; Gmachl, C.; Paiella, R.; Whittaker, E. A.; Hwang, H. Y.; Sivco, D. L.; Baillargeon, J. N.; Cho, A. Y. Free-space optical transmission of multimedia satellite data streams using mid-infrared quantum cascade lasers. *Electron. Lett.* **2002**, *38* (4), 181–183.
- (10) Semenov, A.; Engel, A.; Hübers, H. W.; Il'in, K.; Siegel, M. Spectral cut-off in the efficiency of the resistive state formation caused by absorption of a single-photon in current-carrying superconducting nano-strips. *Eur. Phys. J. B* **2005**, *47* (4), 495–501.
- (11) Semenov, A. D.; Gol'tsman, G. N.; Korneev, A. A. Quantum detection by current carrying superconducting film. *Physica C* **2001**, *351* (4), 349–356.
- (12) Verevkin, A.; Zhang, J.; Sobolewski, R.; Lipatov, A.; Okunev, O.; Chulkova, G.; Korneev, A.; Smimov, K.; Gol'tsman, G. N.; Semenov, A. Detection efficiency of large-active-area NbN single-photon superconducting detectors in the ultraviolet to near-infrared range. *Appl. Phys. Lett.* **2002**, *80* (25), 4687.
- (13) Semenov, A.; Engel, A.; Il'in, K.; Gol'tsman, G.; Siegel, M.; Hübers, H. W. Ultimate performance of a superconducting quantum detector. *Eur. Phys. J.: Appl. Phys.* **2003**, *21* (3), 171–178.
- (14) Ejrnaes, M.; Cristiano, R.; Quaranta, O.; Pagano, S.; Gaggero, A.; Mattioli, F.; Leoni, R.; Voronov, B.; Gol'tsman, G. A cascade switching superconducting single photon detector. *Appl. Phys. Lett.* **2007**, *91* (26), 262509.
- (15) Ejrnaes, M.; Casaburi, A.; Quaranta, O.; Marchetti, S.; Gaggero, A.; Mattioli, F.; Leoni, R.; Pagano, S.; Cristiano, R. Large Signal Amplitude and Bias Range of Cascade Switch Superconducting Nanowire Single Photon Detectors. *IEEE Trans. Appl. Supercond.* **2009**, *19* (3), 323–326.
- (16) Marsili, F.; Najafi, F.; Herder, C.; Berggren, K. K. Electrothermal simulation of superconducting nanowire avalanche photodetectors. *Appl. Phys. Lett.* **2011**, *98* (9), 093507–3.
- (17) A more comprehensive study of the jitter bias dependence in SNSPDs and SNAPs will be reported elsewhere.